

Article

Non-Destructive In Situ Study of Plastic Deformations in Diamonds: X-ray Diffraction Topography and μ FTIR Mapping of Two Super Deep Diamond Crystals from São Luiz (Juina, Brazil)

Giovanna Agrosi^{1,*} , Gioacchino Tempesta¹ , Giancarlo Della Ventura^{2,3},
Mariangela Cestelli Guidi³, Mark Hutchison⁴, Paolo Nimis⁵  and Fabrizio Nestola⁵

¹ Dipartimento di Scienze della Terra e Geoambientali, Università degli Studi “Aldo Moro”, Via Orabona, 4, 70125 Bari, Italy; gioacchino.tempesta@uniba.it

² Dipartimento di Scienze, Università di Roma Tre, I-00146 Rome, Italy; giancarlo.dellaventura@uniroma3.it

³ INFN-LNF, Via Enrico Fermi 40, I-00044 Frascati (Rome), Italy; mariangela.cestelliguidi@lnf.infn.it

⁴ Trigon GeoServices Ltd., 2780 South Jones Blvd, Ste 35-15, Las Vegas, NV 89146, USA; mth@trigon-gs.com

⁵ Dipartimento di Geoscienze, Università degli Studi di Padova, Via G. Gradenigo 6, 35131 Padova, Italy; paolo.nimis@unipd.it (P.N.); fabrizio.nestola@unips.it (F.N.)

* Correspondence: giovanna.agrosi@uniba.it; Tel.: +39-0805-442-610

Academic Editors: Yuri N. Palyanov

Received: 29 June 2017; Accepted: 25 July 2017; Published: 28 July 2017

Abstract: Diamonds from Juina, Brazil, are well-known examples of superdeep diamond crystals formed under sublithospheric conditions and evidence would indicate their origins lie as deep as the Earth’s mantle transition zone and the Lower Mantle. Detailed characterization of these minerals and of inclusions trapped within them may thus provide precious minero-petrogenetic information on their growth history in these inaccessible environments. With the aim of studying non-destructively the structural defects in the entire crystalline volume, two diamond samples from this locality, labelled JUc4 and BZ270, respectively, were studied in transmission mode by means of X-ray Diffraction Topography (XRDT) and micro Fourier Transform InfraRed Spectroscopy (μ FTIR). The combined use of these methods shows a good fit between the mapping of spatial distribution of extended defects observed on the topographic images and the μ FTIR maps corresponding to the concentration of N and H point defects. The results obtained show that both samples are affected by plastic deformation. In particular, BZ270 shows a lower content of nitrogen and higher deformation, and actually consists of different, slightly misoriented grains that contain sub-grains with a rounded-elongated shape. These features are commonly associated with deformation processes by solid-state diffusion creep under high pressure and high temperature.

Keywords: super deep diamonds; structural defects; X-ray diffraction topography; infrared spectroscopy; plastic deformation

1. Introduction

Diamond shows brittle behaviour at low temperatures, but with increasing temperature it softens considerably and plastic flow arises. Most natural diamonds experience post-growth plastic deformation during their period of residence in the mantle, which can be observed, for example, in birefringence patterns. Several different features of deformation can be found in lithospheric and sub-lithospheric diamonds, depending on both extrinsic and intrinsic factors. Temperature, pressure, time of residence and applied stress are extrinsic factors, whereas the different growth defects such as dislocations, twins, stacking faults, point defects and inclusions represent the intrinsic factors. The

major difference between the plastic deformation of sub-lithospheric diamonds compared to that of lithospheric diamonds is that the former grow at much higher pressure and temperature, and in a mantle characterized by convection, whereas lithospheric diamonds grow in a stiffer mantle host that is not undergoing convection. Consequently, the plastic deformation of diamonds originating from the Earth's sub-lithospheric mantle is much more complex and can only be investigated in detail by combining different techniques.

In diamond research, X-ray Diffraction Topography (XRDT) and micro-Fourier Transform InfraRed Spectroscopy (μ FTIR) are useful tools for investigating extended and point lattice defects, respectively, in transmission mode [1]. With the aim of contributing to the characterization of plastic deformations in sub-lithospheric diamonds, a multi-methodological and non-destructive approach, combining both XRDT and μ FTIR, was used here to study two superdeep diamond crystals from São Luiz (Juina, Brazil) that had solid inclusions still trapped within them. This integrated methodological analysis provides a sort of “diamond mapping”, which visualizes the growth and post-growth defects, totally preserving the sample.

XRDT is a non-destructive technique that has been extensively used to obtain images of structural defects with a resolution limit of a few μm . In particular, this method has been employed to control the growth process of synthetic crystals used as electronic devices, to characterize their crystalline quality and their physical properties, and to obtain information on crystal growth mechanisms [2,3]. Recently, XRDT has been successfully employed in Earth Science to study the growth history of tourmalines, garnets, and beryl [4–7]. XRDT in transmission mode (Laue geometry) is particularly suitable for studying structural defects in diamonds, because the low attenuation coefficient of the X-ray beam makes this mineral matrix highly transparent to X-rays. This allows investigation of the structural defects of the whole sample [8,9] instead of just its surface, as is the case with cathodoluminescence. Indeed, this peculiarity allows for imaging of the strain fields associated with defects, without the necessity of cutting the sample into slices. The results obtained in two previous studies by XRDT on diamonds from the Finsch mine, South Africa [10], and from the Udachnaya kimberlite, Siberia [11], provided significant minero-petrogenetic insights into their growth conditions. In the first case, a reconstruction of the growth history of a diamond characterized by the development of sub-individuals (twinned and untwinned) was possible. The data showed how the development of sub-grains could be related to a relaxation phenomenon following the stress caused by the incorporation of large pyrope and orthoenstatite inclusions; a complete discrimination between growth and post-growth defects was also performed. The second study contributed to the debate on the criteria required to establish the genetic nature of inclusions in diamonds, supporting the hypothesis of [12] that diamond-imposed morphology can be caused by a processes of selective partial dissolution at the interface between the diamond and, in this case, its olivine inclusions. To the best of our knowledge, XRDT is used in the present paper for the first time to analyse the structural defects of superdeep diamonds from São Luiz.

FTIR spectra are sensitive to the presence of point defects, in particular nitrogen and its aggregation patterns (N-type defects), that are characterized by different absorption bands in the 1000 to 1500 cm^{-1} wavenumber range [13,14]. FTIR also allows for evaluation of the presence of H defects by using an absorption peak centred at $\approx 3107 \text{ cm}^{-1}$. The distribution of these defects in diamond samples is rarely homogenous, and its zoning patterns depend on multiple episodes under changing crystal growth conditions [15–19]. Finally, FTIR spectroscopy allows for studying, with relatively high-resolution (nominally 5–10 μm when using a bi-dimensional FPA detector), the distribution of a target molecule across a sample [20]. FTIR spectroscopy is a relatively well known analytical tool for diamonds and has been extensively used to characterize impurities and/or inclusions typically present in these materials [21–24]. In the diamond literature, the mapping of single FTIR absorption bands are typically reported [1,25–29] to represent the distribution of the selected defect, obtained by plotting the intensity measured at a specific wavenumber or the integrated peak area. Resulting maps can generate a better understanding of the diamond growth environment.

2. Results

2.1. Samples

The samples studied in this work labelled BZ270 (Figure 1a) and JUc4 (Figure 1b), respectively, are from São Luiz (Juina, Brazil; JUc4 from WGS84 Zone 21S 261000; 8708000 and BZ270 from an unknown alluvial location in the wider area); they are broken crystals up to 6–7 mm in maximum dimension, exhibiting an irregular morphology and a brownish color. This color in diamond is commonly related to vacancy clusters, produced by plastic deformation of the crystal structure [30], as recently confirmed also by spectroscopic studies [31]. Both diamond crystals are partially flattened along the (111) plane. Optical observations revealed anomalous birefringence and the presence of dark and opaque inclusions that, from data published in a previous work [32], are mostly identified as ferro-periclase. These inclusions are very large in size (some hundreds of μm), although the BZ270 sample also exhibits smaller inclusions of as yet uncertain origin.



Figure 1. Optical micrographs of diamond crystals: (a) BZ270; (b) JUc4.

2.2. XRDT

The X-ray topographic images show that both diamonds exhibit an extensive plastic deformation that precludes simultaneous X-ray diffraction of the whole crystal. Nevertheless, despite their common provenance and similarity of inclusions, they show a significantly different type of post-growth deformation.

According to the XRDT data, diamond BZ270 consists of an aggregate of slightly misoriented grains (G) that are not visible simultaneously at the individual angular settings due to the different diffraction vector (Figure 2). Topographs taken with a diffraction vector of type $\langle 111 \rangle$ (Figure 2a,b) exhibit a misalignment of about 1° between 2 different portions, irrespective of grains and growth sector. The boundary between these portions (CP in the Figure) belongs to the (-111) plane and represents a typical cleavage plane, interpreted to be due to post-growth brittle deformation (Figure 2).

In the topographs of Figure 2c,d, the diffraction contrast corresponding to two slightly different angular settings of the same diffraction vector ($\mathbf{g} = 2-20$) shows that the diamond region containing the ferro-periclase inclusions is really a grain (G) that is differently oriented with respect to the other diamond regions. In the Figure 2c G is out of contrast, whereas in Figure 2d G is in diffraction contrast and the surrounding grains are out of contrast.

In Figure 2e,f two slightly different angular setting (few seconds of arc) of the same diffraction vector ($\mathbf{g} = -131$) show that the grain labelled G is out of contrast together with other portions corresponding to further grains. It is worth noting that the apparent different size and shape of the topographic images and the different grains are due to the projection effect under the different angular setting of the different topographs. Within the same grains, patchy sub-grains exhibiting a rounded and elongated drop shape are visible (SG).

The diffraction contrast analysis shows that the grains and the subgrains are visible mainly under the reflections $\mathbf{g} = 2-20$ and $\mathbf{g} = -131$, because of non-simultaneous diffraction conditions for each of them (Figure 2c–f). This finding implies a condition of extinction for some grains and subgrains with respect to the others under these reflections. Applying the extinction criteria, the common direction that satisfies in both cases the extinction corresponds to the (-112) direction.

In Figure 3, an optical micrograph taken under crossed polars of the enlarged detail of the grain (G) containing large inclusions of ferro-periclase is compared with the corresponding topographic image. Comparison reveals that the topographic image exhibits a similar shape of diffraction contrast corresponding to the inclusions (marked by numbers) and the subgrains (SG).

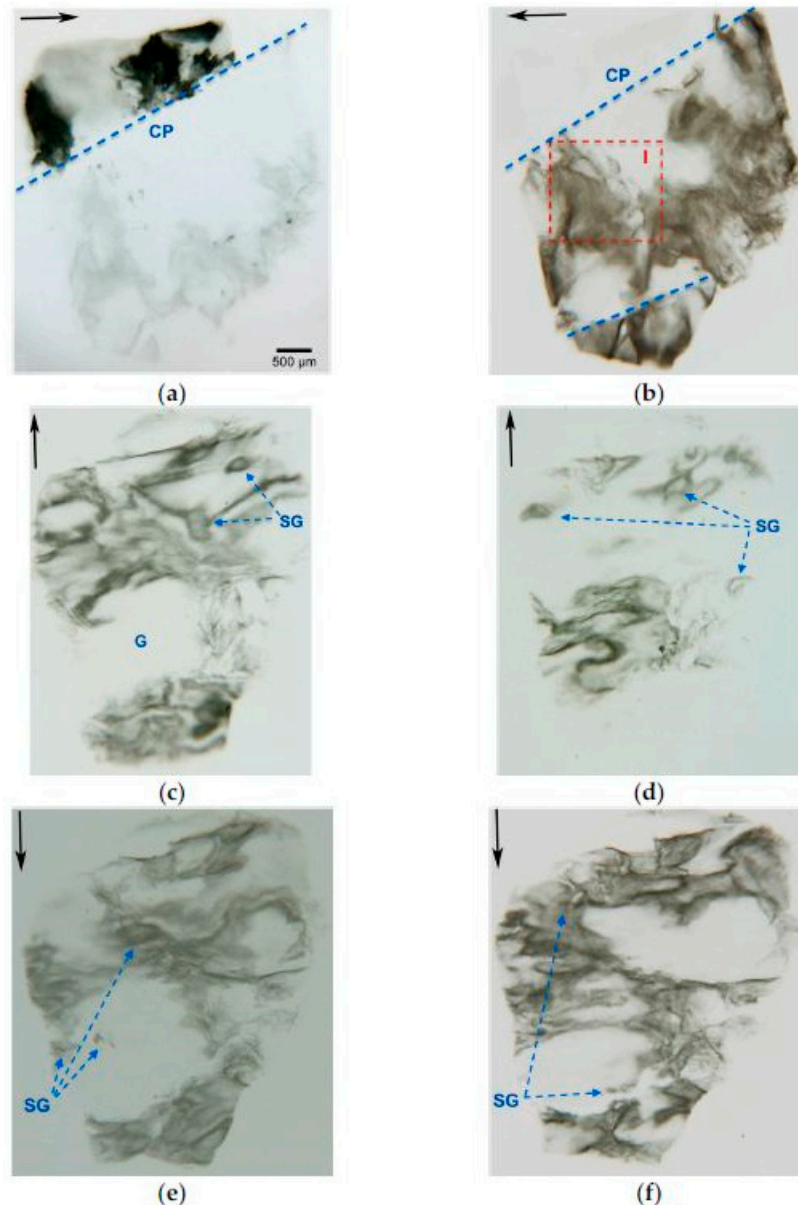


Figure 2. X-ray topographic images ($\text{MoK}\alpha_1$) of diamond B7270. The black arrows represent the diffraction vector projection \mathbf{g} . CP: Cleavage plane; G: misoriented grains; SG: sub-grains indicated by dashed blue arrows; I: area magnified in Figure 3. The directions of the diffraction projection vector are: (a) $\mathbf{g} = -1-11$; (b) $\mathbf{g} = 11-1$; (c,d) $\mathbf{g} = 2-20$; (e,f) $\mathbf{g} = -131$. The apparent different size and shape of the topographic images is due to the projection effect of the angular setting for the different reflections.

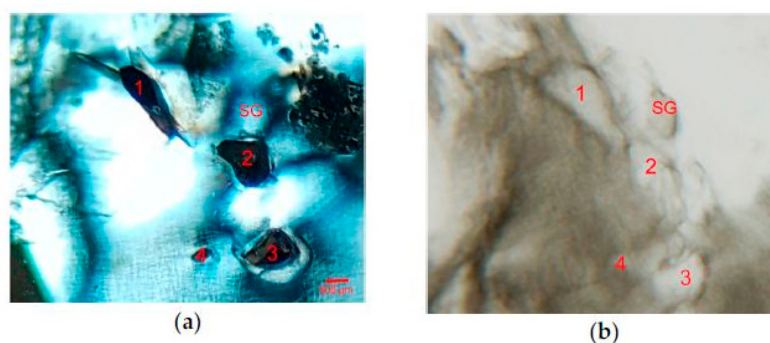


Figure 3. Enlarged portion of diamond B7270 surrounded by the red dashed line in Figure 2b. (a) Optical micrograph taken under crossed polars; (b) X-ray topographic image ($\text{MoK}\alpha_1$). The red numbers tag the inclusions and the corresponding contrasts. Note the similar shape of the inclusions and sub-grain (SG).

XRDT images acquired on JUc4 show different plastic deformation patterns: this sample is shown to be a single crystal, extensively plastically deformed, while no subgrains are visible. The diffraction contrast of topographs taken under the reflection with $\mathbf{g} = -220$ (Figure 4a,b) exhibits laminations along different slip systems that are out of contrast in the topograph taken with the diffraction vector $\mathbf{g} = -1-11$ (Figure 4c). The interaction of the different slip systems and the initial bending of lattice planes determine a resultant elongated strain (Figure 4).

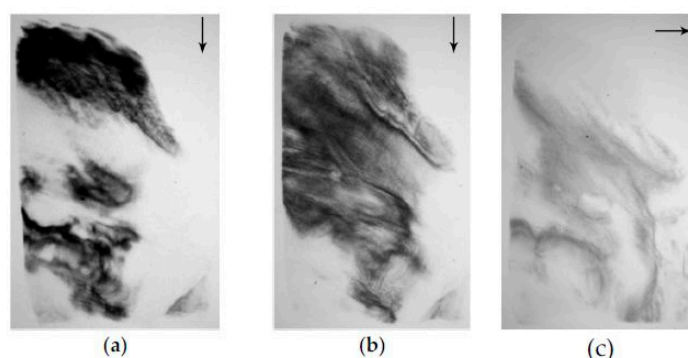


Figure 4. X-ray topographic images ($\text{MoK}\alpha_1$) of diamond JUc4. The black arrows represent the diffraction vector projection \mathbf{g} . (a) $\mathbf{g} = -220$; (b) $\mathbf{g} = -220$; (c) $\mathbf{g} = -1-11$. The apparent different size and shape of the topographic images of the sample are due to the projection effect of the angular setting for the different reflections.

2.3. μFTIR

In Figure 5a two selected single-point spectra ($50\ \mu\text{m}$ beam dimension) collected on samples BZ270 and JUc4, respectively, are compared. The broad and convolute absorption extending from 2700 to $1700\ \text{cm}^{-1}$ is due to the diamond matrix, while the broad absorption in the range 1400 – $1000\ \text{cm}^{-1}$ is due to the different N defects (for type I diamonds). In more detail, the different peaks in this region allow differentiation of the possible N-related defects and clusters within the structure, i.e., isolated vs. aggregated N impurities [13] (for assistance following the discussion below, the N impurity region for sample JUc4 is enlarged in Figure 5b). In particular, the spectrum of diamond JUc4 shows two very weak peaks at 1405 and $1385\ \text{cm}^{-1}$, respectively, an intense and a sharp peak at $1330\ \text{cm}^{-1}$, and a very broad and intense absorption at $1170\ \text{cm}^{-1}$ (Figure 5b). Two broad and relatively weak absorptions can finally be resolved at 1095 and $1010\ \text{cm}^{-1}$, respectively (Figure 5b). The spectra of Figure 5a show that the examined samples have significantly different N contents: while JUc4 has a well resolvable nitrogen

absorption, BZ270 has a very low, barely appreciable absorption in the 1400–1000 cm^{-1} range. Based on the N-band nomenclature given in [13] the most intense peaks at 1330 and 1170 cm^{-1} can be assigned to N impurities aggregated in clusters of four atoms and associated structural vacancies (B defects). N impurities aggregated in pairs (A defects) are characterized by an intense band at 1282 cm^{-1} ; this band is absent from the spectrum of both examined diamonds. The weak peak at 1385 cm^{-1} can be assigned to B2 aggregates or platelets. This peak is usually found paired to the band of 1170 cm^{-1} corresponding to B aggregates [33]. The broad band at 1095 can be assigned to the overlapping of two characteristic bands: the first at 1090 cm^{-1} corresponding to the A and B defects [34], and the second (1100 cm^{-1}) that could be ascribed to the dislocation loop remaining from the decomposition of the platelets under plastic deformation [35]. Both samples, in addition, show a weak but resolvable peak assigned to the presence of H impurities, centered at 3107 cm^{-1} (Figure 5a). The hydrogen impurity peak is barely appreciable in sample BZ270 (Figure 5a), while it is relatively prominent in sample JUc4. The different intensity associated with the N absorbance in Figure 5a cannot be used for quantitative evaluations, due to the different thickness of the studied crystal sections. Previous direct analytical data carried out destructively on small fragments extracted from both samples (Hutchison, unpublished data) gave different N contents for different fragments from the same sample, suggesting an inhomogeneous N concentration; the average total N for JUc4 is about 64.8 ppm while being 17.8 ppm for BZ270. Based on all available data, sample JUc4 can be classified a type IaB diamond, while based only on its average N content, under 50 ppm, BZ270 could be classified a type IIa diamond, but locally the amount of the detected B defects suggests a classification of a type IaB.

The FTIR maps integrated over the range 1400–1000 cm^{-1} for N defects and over the range 3120–3075 cm^{-1} for H defects are shown in Figures 6 and 7. These maps were superimposed on the optical micrographs of the samples, and care was taken to make the maps transparent. The maps allow a better understanding of the heterogeneous distribution of N in JUc4 and BZ270. Notably, on both samples, the spatial distribution of the intensity associated with H defects is always related to that of N defects. In particular, for BZ270 the maps of total N defects (Figure 6a) and H defects (Figure 6b) show a singular distribution in the micro-domains, which apparently correspond to the grain and subgrains observed in the topographic image (cf. G and SG in Figure 2). In particular, the grain labelled G, which contains the ferro-pericline inclusions, appears completely free of N and H defects. Conversely, the FTIR spectroscopic maps of diamond JUc4 show a clear concentric zoning of total N defects (Figure 7), confirming that this diamond can be interpreted as a single crystal. However, also for this sample, the elongated shape of the zoning pattern reproduces the deformation observed on the topographic images.

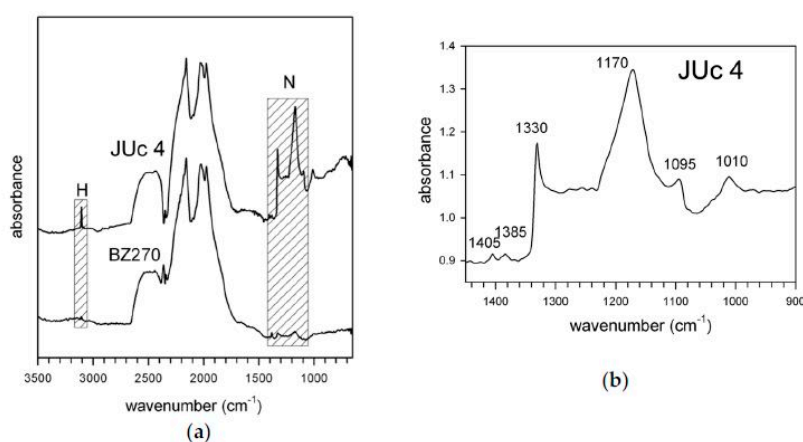


Figure 5. (a) Selected FTIR single-point spectra (50 μm beam size) of the studied samples. The absorbance regions of H and N impurities, respectively, are indicated. Spectra normalized to the diamond absorption. (b) Enlargement of the spectrum of JUc4 in the N impurity region; for explanations, see text.

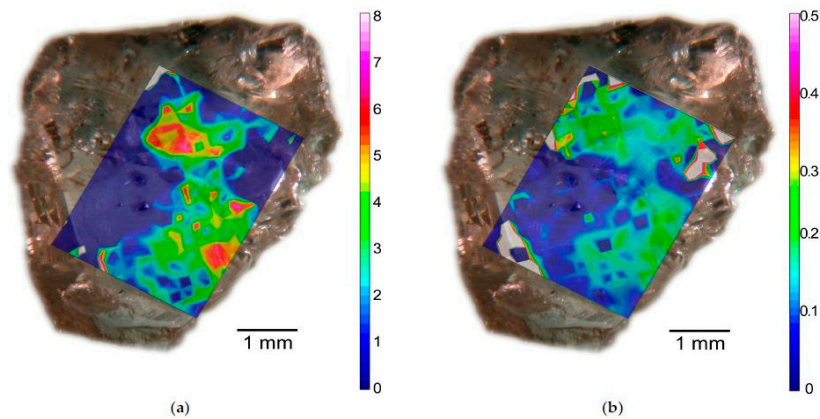


Figure 6. FTIR maps of diamond BZ270. (a) N concentration, integration range $1400\text{--}1000\text{ cm}^{-1}$; (b) H defects, integration range $3120\text{--}3075\text{ cm}^{-1}$. Both maps were taken with a $50\text{ }\mu\text{m}^2$ beam at step of $50\text{ }\mu\text{m}$. The spectroscopic maps are superimposed on the optical micrograph of Figure 1. The color scale is proportional to the measured intensity, from blue (zero intensity) to red/whitish (max intensity).

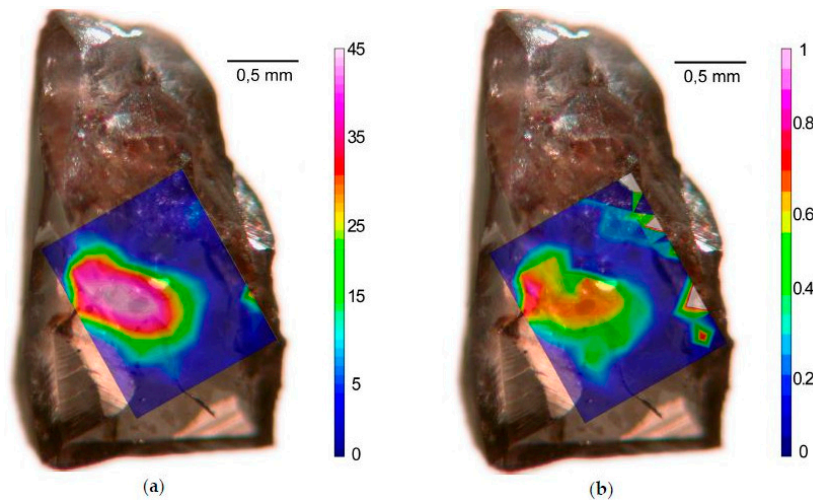


Figure 7. FTIR maps of diamond JUc4. (a) N concentration, integration range $1400\text{--}1000\text{ cm}^{-1}$; (b) H defects, integration range $3120\text{--}3075\text{ cm}^{-1}$. Both maps were taken with a $50\text{ }\mu\text{m}^2$ beam at step of $50\text{ }\mu\text{m}$. The spectroscopic maps are superimposed to the optical micrograph of Figure 1. The color scale is proportional to the measured intensity, from blue (zero intensity) to red/whitish (max intensity).

3. Discussion

The XRDT images are remarkably similar to FTIR maps. The topographs clearly show a strained zone at the boundary separating the domains with different concentrations of N defects, suggesting a migration of point defects during the plastic deformation process. More in detail, the results obtained show that the diamonds studied here experienced different growth and post-growth history.

The sample labelled BZ270 consists of an aggregate of misoriented grains. However, formation of this diamond from multiple simultaneous growth centers can be ruled out. The grain, labelled G in the topographs, containing large inclusions of ferro-periclase and lacking N and H point defects, is different from the others and can be considered as the product of an early stage of growth.

A second step of growth was characterized by the development and aggregation of different grains with the entrapment of a second generation of small inclusions, possibly along some grain boundaries. These grains exhibit a low content of point defects even if their concentration is significantly higher

than in the early stage, suggesting modified growth conditions. Episodes of partial dissolution could be invoked to explain the irregular shape of the grains.

After the diamond development, a stage of plastic deformation characterized by the formation of subgrains occurred. This type of plastic deformation has never been reported for diamonds from São Luiz. This could be related to the fact that diamonds from São Luiz have been studied by XRDT in transmission mode for the first time in the present work. Actually, previous studies were performed using mainly cathodoluminescence (surface analyses), and the most common plastic deformation features found were lamination and thus micro-twinning along {111} planes [36]. It is well known that the formation of the twinned micro-lamellae is an important mechanism for deformation accommodation in diamond [37]. Previous high-pressure and high-temperature (HP-HT) experiments carried out on synthetic diamonds suggested that the {111} micro-twins begin to form under a range of P and T conditions typical for the upper mantle [26,38,39]. Howell et al. (2012) [26] showed that further differential stress brings a continuous crystal bending that produces the formation of subgrains. In particular, when multiple slip systems {111} <110> occur simultaneously, a rotation of subgrains arises around <112> axes. However, owing to the quantitative estimation of P and T and/or applied stress responsible for this further deformation, is difficult to estimate for natural diamonds, because the inherent growth defects of the diamond crystal, mechanical properties, and degree of homogeneity of the medium in which the crystal is deformed are unknown [40]. The analysis of diffraction contrasts of this study confirms that the subgrains observed in BZ270 are rotated around the (−112) direction. Commonly, a deformation process by dislocation movement causes a polygonal shape of subgrains [41–43]. The lobate shape of subgrains found in BZ270 suggests a formation mechanism by solid state diffusion creep under HTHP conditions similar to sublithospheric mantle conditions. When a crystal deforms by diffusion creep to accommodate space problems from simultaneous movement of whole grains along grain boundaries, a process of superplastic-like flow occurs [44,45]. This process could also explain the nitrogen aggregation state found by FTIR. The similar shape of diffraction contrast between the inclusions and the subgrains (Figure 3) suggests that the plastic deformation could have also affected the inclusions. An important topic, which can be considered in the future, regards the study of the different behavior of diamond and ferro-periclase under the same stress and the mechanical effects at the interface between diamond and non-diamond inclusions.

Finally, during the ascent of the diamond or during its eruption, the diamond BZ270 experienced brittle deformation with CP formation.

Conversely, diamond JUc4 consists of a single N-zoned crystal with a higher amount of N with respect to the sample BZ270. FTIR maps reveal that also for this sample the concentration of N follows the shape of plastic deformation. No subgrains were found but a polygonised network of different systems of lamination with an elongated shape of deformation can be ascribed to a lower level of plastic deformation compared to BZ270. This difference might be related to the different content of nitrogen and/or to a different density of growth defects, as well as to dislocations. In addition, different types of stress might generate different deformation features.

The plastic deformation found in the studied samples and the differences found between BZ270 and JUc4 are consistent with derivation of these diamonds from a heterogeneous sublithospheric mantle characterized by convection.

4. Materials and Methods

4.1. XRDT

The diamonds were investigated by XRDT in transmission geometry, using a conventional source, at the University of Bari (Italy). The technique, developed by [46], is a non-destructive imaging technique, sensitive to the strain associated with extended defects, that yields the spatial distribution and full characterization of the crystal defects in the whole sample volume. The topographs taken with Laue geometry were carried out using a Rigaku camera (Rigaku International Corporation,

Tokyo, Japan) with monochromatic radiation ($\text{MoK}\alpha_1$) and with a micro-focus X-ray tube. XRDT is particularly suitable for the non-destructive investigation of the structural defects in diamond because of its low X-ray attenuation coefficient that allows the optimum kinematic diffraction condition $\mu t \approx 1$ (μ = linear absorption coefficient; t = crystal thickness) to be made, minimizing the X-ray absorption. Spatial resolution using these conditions is about 1–2 μm . The diffraction contrast was recorded on high-resolution photographic films (SR Kodak). Characterization of the structural defects was performed by applying the extinction criteria to their diffraction contrasts, according to kinematic and dynamic X-ray diffraction theories [47]. The detailed XRDT procedures used in this study are given in Agrosi, et al. (2016) [11].

4.2. μFTIR

Micro-FTIR maps were obtained by using a Bruker Hyperion 3000 microscope fitted to a Vertex V70 (both Bruker Optics, Ettlingen, Germany) optical bench, a Globar IR source, and a KBr broadband beamsplitter. The FTIR microscope was equipped with a 15X Schwarzschild objective, a motorized XY stage, and an LN_2 cooled MCT detector. The data were collected at a nominal resolution of 4 cm^{-1} ; 128 spectra were averaged for both spectrum and background. The analytical grid covered continuously the mapped area, using a square aperture of $50\ \mu\text{m}^2$ at step of $50\ \mu\text{m}$. The diamond sample was initially placed on a ZnSe sample holder, but preliminary tests showed a significant periodic disturbance in the pattern (interference fringes) due to the interference of the IR beam exiting from the sample. This disturbance hindered any reliable integration of the absorbance peaks, therefore to overcome this problem, a thin layer of powdered KBr was inserted between the diamond crystal and the ZnSe sample holder. This shrewdness was effective in eliminating the interference fringes from the patterns. Spectroscopic maps were obtained by integrating the target peak as indicated in the text. Additional information on the method can be found in [20].

5. Conclusions

Although the diamonds studied both derive from the same area of São Luiz and contain the same types of inclusions, they show a heterogeneity of growth and post-growth history that can be explained only if the crystallization and deformation processes occurred within a heterogeneous sublithospheric mantle characterized by convecting movement. This study suggests that the reconstruction of the different stages of growth and plastic deformation of the studied diamonds by means of the analyses of structural defects should be preliminary to the studies on the inclusions in order to obtain robust conclusions on the inclusion–host growth relationships and their minero-petrogenetic implications.

Acknowledgments: The research was supported by ERC Starting Grant INDIMEDEA (grant number 307322) awarded to Fabrizio Nestola, University of Padova (Italy).

Author Contributions: Giovanna Agrosi, Gioacchino Tempesta, and Fabrizio Nestola conceived and designed the experiments; Mark Hutchison contributed the diamond samples; Giovanna Agrosi, Gioacchino Tempesta, Giancarlo Della Ventura, and Mariangela Cestelli Guidi performed the experiments; Giovanna Agrosi, Gioacchino Tempesta, Giancarlo Della Ventura, Mariangela Cestelli Guidi, Mark Hutchison, Paolo Nimis, and Fabrizio Nestola analyzed the data and oversaw the manuscript; Giovanna Agrosi wrote the paper.

Conflicts of Interest: The authors declare no conflict of interest.

References

1. Shiryaev, A.A.; Fisenko, A.V.; Vlasov, I.I.; Semjonova, L.F.; Nagel, P.; Schuppler, S. Spectroscopic study of impurities and associated defects in nanodiamonds from Efremovka (CV3) and Orgueil (CI) meteorites. *Geochim. Cosmochim. Acta* **2011**, *75*, 3155–3166. [[CrossRef](#)]
2. Bowen, D.K.; Tanner, B.K. *High Resolution X-ray Diffractometry and Topography*; CRC Press: Bristol, UK, 2005.
3. Agrosi, G.; Tempesta, G.; Capitani, G.C.; Scandale, E.; Siche, D. Multi-analytical study of syntactic coalescence of polytypes in a 6H–SiC sample. *J. Cryst. Growth* **2009**, *311*, 4784–4790. [[CrossRef](#)]

4. Agrosi, G.; Bosi, F.; Lucchesi, S.; Melchiorre, G.; Scandale, E. Mn-tourmaline crystals from island of Elba (Italy): Growth history and growth marks. *Am. Mineral.* **2006**, *91*, 944–952. [[CrossRef](#)]
5. Agrosi, G.; Scandale, E.; Tempesta, G. Growth marks of titanian-andradite crystals from Colli Albani (Italy). *Period. Di Mineral.* **2011**, *80*, 89–104.
6. Tempesta, G.; Scandale, E.; Agrosi, G. Striations and hollow channels in rounded beryl crystals. *Period. Di Mineral.* **2011**, *79*, 75–87.
7. Pignatelli, I.; Giuliani, G.; Ohnenstetter, D.; Agrosi, G.; Mathieu, S.; Morlot, C.; Branquet, Y. Colombian trapiche emeralds: Recent advances in understanding their formation. *Gems Gemol.* **2015**, *51*, 222–259. [[CrossRef](#)]
8. Moore, M. Imaging diamond with X-rays. *J. Phys. Condens. Matter* **2009**, *21*, 364217. [[CrossRef](#)] [[PubMed](#)]
9. Moore, M.; Nailer, S.G.; Wierzchowski, W.K. Optical and X-ray topographic studies of dislocations, growth-sector boundaries, and stacking faults in synthetic diamonds. *Crystals* **2016**, *6*, 71. [[CrossRef](#)]
10. Agrosi, G.; Tempesta, G.; Scandale, E.; Harris, J.W. Growth and post-growth defects of a diamond from Finsch mine (South Africa). *Eur. J. Mineral.* **2013**, *25*, 551–559. [[CrossRef](#)]
11. Agrosi, G.; Nestola, F.; Tempesta, G.; Bruno, M.; Scandale, E.; Harris, J.W. X-ray topographic study of a diamond from Udachnaya: Implications for the genetic nature of inclusions. *Lithos* **2016**, *248*, 153–159. [[CrossRef](#)]
12. Nestola, F.; Nimis, P.; Angel, R.J.; Milani, S.; Bruno, M.; Prencipe, M.; Harris, J.W. Olivine with diamond-imposed morphology included in diamonds. Syngeneses or protogeneses? *Int. Geol. Rev.* **2014**, *56*, 1658–1667. [[CrossRef](#)]
13. Breeding, C.M.; Shigley, J.E. The “type” classification system of diamonds and its importance in gemology. *Gems Gemol.* **2009**, *45*, 96–111. [[CrossRef](#)]
14. Kaminsky, F.V.; Khachatryan, G.K. The relationship between the distribution of nitrogen impurity centres in diamond crystals and their internal structure and mechanism of growth. *Lithos* **2004**, *77*, 255–271. [[CrossRef](#)]
15. De Vries, D.W.; Pearson, D.G.; Bulanova, G.P.; Smelov, A.P.; Pavlushin, A.D.; Davies, G.R. Re–Os dating of sulphide inclusions zonally distributed in single Yakutian diamonds: Evidence for multiple episodes of Proterozoic formation and protracted timescales of diamond growth. *Geochim. Cosmochim. Acta* **2013**, *120*, 363–394. [[CrossRef](#)]
16. Griffin, B.J.; Bulanova, G.P.; Taylor, W.R. CL and FTIR mapping of nitrogen content and hydrogen distribution in diamonds from the Mir pipe—Constraints on growth history. Extended Abstracts of the 6th International Kimberlite Conference, Novosibirsk, Russia, 7–11 August 1995.
17. Palot, M.; Pearson, D.G.; Stachel, T.; Harris, J.W.; Bulanova, G.P.; Chinn, I. Multiple growth episodes or prolonged formation of diamonds? Inferences from infrared absorption data. In Proceedings of the 10th International Kimberlite Conference, New Delhi, India, 6–10 February 2012.
18. Pearson, D.G.; Shirey, S.B.; Bulanova, G.P.; Carlson, R.W.; Milledge, H.J. Re–Os isotope measurements of single sulfide inclusions in a Siberian diamond and its nitrogen aggregation systematics. *Geochim. Cosmochim. Acta* **1999**, *63*, 703–711. [[CrossRef](#)]
19. Taylor, W.R.; Bulanova, G.P.; Milledge, H.J. Quantitative nitrogen aggregation study of some Yakutian diamonds: Constraints on the growth, thermal and deformation history of peridotitic and eclogitic diamonds. Extended Abstracts of the 6th International Kimberlite Conference, Novosibirsk, Russia, 7–11 August 1995.
20. Della Ventura, G.; Marcelli, A.; Bellatreccia, F. SR-FTIR Microscopy and FTIR Imaging in the Earth Sciences. *Rev. Mineral. Geochem.* **2014**, *78*, 447–480. [[CrossRef](#)]
21. Kaminsky, F.V.; Khachatryan, G.K. Characteristics of nitrogen and other impurity in diamond, as revealed by infrared absorption data. *Can. Mineral.* **2001**, *39*, 1735–1745. [[CrossRef](#)]
22. Hainschwang, T.; Notari, F.; Fritsch, E.; Massi, L. Natural, untreated diamonds showing the A, B and C infrared absorptions (“ABC diamonds”), and the H₂ absorption. *Diam. Relat. Mater.* **2006**, *15*, 1555–1564. [[CrossRef](#)]
23. Gaillou, E.; Post, J.E.; Rost, D.; Butler, J.E. Boron in natural type IIb blue diamonds; chemical and spectroscopic measurements. *Am. Mineral.* **2012**, *97*, 1–18. [[CrossRef](#)]
24. Palot, M.; Jacobsen, S.D.; Townsend, J.P.; Nestola, F.; Marquardt, K.; Miyajima, N.; Harris, J.W.; Stachel, T.; McCammon, C.A.; Pearson, D.G. Evidence for H₂O-bearing fluids in the lower mantle from diamond inclusion. *Lithos* **2016**, *265*, 237–243. [[CrossRef](#)]
25. Bulanova, G.P.; Pearson, D.G.; Hauri, E.H.; Griffin, B.J. Carbon and nitrogen isotope systematics within a sector-growth diamond from the Mir kimberlite, Yakutia. *Chem. Geol.* **2002**, *188*, 105–123. [[CrossRef](#)]

26. Howell, D.; O'Neill, C.J.; Grant, K.J.; Griffin, W.L.; O'Reilly, S.Y.; Pearson, N.J.; Stern, R.A.; Stachel, T. Platelet development in cuboid diamonds: Insights from micro-FTIR mapping. *Contrib. Mineral. Petrol.* **2012**, *164*, 1011–1025. [[CrossRef](#)]
27. Lu, T.; Chen, H.; Qiu, Z.; Zhang, J.; Wei, R.; Ke, J.; Sunagawa, I.; Stern, R.; Stachel, T. Multiple core growth structure and nitrogen abundances of diamond crystals from Shandong and Liaoning kimberlite pipes, China. *Eur. J. Mineral.* **2012**, *24*, 651–656. [[CrossRef](#)]
28. Spetsius, Z.V.; Bogush, I.N.; Kovalchuk, O.E. FTIR mapping of diamond plates of eclogitic and peridotitic xenoliths from the Nyurbinskaya pipe, Yakutia: Genetic implications. *Russ. Geol. Geophys.* **2015**, *56*, 344–353. [[CrossRef](#)]
29. Kohn, S.C.; Speich, L.; Smith, C.B.; Bulanova, G.P. FTIR thermochronometry of natural diamonds: A closer look. *Lithos* **2016**, *265*, 148–158. [[CrossRef](#)]
30. Smith, E.M.; Helmstaedt, H.H.; Flemming, R. Survival of Brown Colour in Diamond during Storage in the Subcontinental Lithospheric Mantle. *Can. Mineral.* **2010**, *48*, 571–582. [[CrossRef](#)]
31. Yuryeva, O.P.; Rakhmanova, M.I.; Zedgenizov, D.A. Nature of type IaB diamonds from the Mir kimberlite pipe (Yakutia): Evidence from spectroscopic observation. *Phys. Chem. Miner.* **2017**, 1–3. [[CrossRef](#)]
32. Mikhail, S.; Howell, D.; Hutchinson, M.; Verchovsky, A.B.; Warburton, P.; Southworth, R.; Milledge, H.J. Constraining the internal variability of carbon and nitrogen isotopes in diamonds. *Chem. Geol.* **2014**, *366*, 14–23. [[CrossRef](#)]
33. Brozel, M.R.; Evans, T.; Stephenson, R.F. Partial dissociation of nitrogen aggregates in diamond by high temperature-high pressure treatments. *Proc. R. Soc. Lond. A* **1978**, *361*, 109–127. [[CrossRef](#)]
34. Sutherland, G.B.; Blackwell, D.E.; Simeral, W.G. The Problem of the Two Types of Diamond. *Nature* **1954**, *174*, 901–904. [[CrossRef](#)]
35. Collins, A.T. *In the Physics of Diamond. Course CXXXV, Proc. Int. School Physics*; IOS Press: Amsterdam, The Netherlands, 1997; p. 195.
36. Hutchinson, M.T.; Cartigny, P.; Harris, J.W. Carbon and nitrogen compositions and physical characteristics of transition zone and lower mantle diamonds from São Luiz, Brazil. In Proceedings of the 7th International Kimberlite Conference, Red Roof Design, Cape Town, South Africa, 11–17 April 1998.
37. Titkov, S.V.; Krivovichev, S.V.; Organova, N.I. Plastic deformation of natural diamonds by twinning: Evidence from X-ray diffraction studies. *Mineral. Mag.* **2012**, *76*, 143–149. [[CrossRef](#)]
38. Yu, X.; Raterron, P.; Zhang, J.; Xhijun, L.; Liping, W.; Zhao, Y. Constitutive Law and Flow Mechanism in Diamond Deformation. *Sci. Rep.* **2012**, *2*, 876. [[CrossRef](#)] [[PubMed](#)]
39. Agrosi, G.; Tempesta, G.; Mele, D.; Allegretta, I.; Terzano, R.; Shirey, S.; Pearson, D.G.; Nestola, F. Multi-analytical approach for non-destructive analyses of a diamond from Udachnaya and its trapped inclusions: the first report of (Fe,Ni)_{1+x}S mackinawite sulfide in diamonds. *Am. Mineral.* **2017**, in press.
40. Shiryaev, A.A.; Frost, D.J.; Langenhorst, F. Impurity diffusion and microstructure in diamonds deformed at high pressures and temperatures. *Diam. Relat. Mater.* **2007**, *16*, 503–511. [[CrossRef](#)]
41. Friedel, G. *Dislocations*; [Russian translation]; Mir: Moscow, Russia, 1967.
42. Hirth, J.P.; Lothe, J. *Theory of Dislocation*; [Russian translation]; Atomizdat: Moscow, Russia; McGraw-Hill: New York, NY, USA, 1972.
43. Sumida, N.; Lang, A.R. Cathodoluminescence evidence of dislocation interactions in diamond. *Philos. Mag. A* **1981**, *43*, 1277–1287. [[CrossRef](#)]
44. Hiraga, T.; Miyazaki, T.; Tasaka, M.; Yoshida, H. Mantle superplasticity and its self-made demise. *Nature* **2010**, *468*, 1091–1094. [[CrossRef](#)] [[PubMed](#)]
45. Ohuchi, T.; Kawazoe, T.; Higo, Y.; Funakoshi, K.; Suzuki, A.; Kikegawa, T.; Irifune, T. Dislocation-accommodated grain boundary sliding as the major deformation mechanism of olivine in the Earth's upper mantle. *Sci. Adv.* **2015**, *1*, e1500360. [[CrossRef](#)] [[PubMed](#)]
46. Lang, A.R. The projection topograph: A new method in X-ray diffraction microradiography. *Acta Cryst.* **1959**, *2*, 249–250. [[CrossRef](#)]
47. Authier, A.; Zarka, A. X-ray topographic study of the real structure of minerals. In *Advanced Mineralogy*; Marfunin, A.S., Ed.; Springer-Verlag: Berlin, Germany, 1994; pp. 221–233.

